AIMS Materials Science, 10(3): 541–555.
DOI: 10.3934/matersci.2023030
Received: 21 April 2023
Revised: 31 May 2023
Accepted: 12 June 2023
Published: 30 June 2023

http://www.aimspress.com/journal/Materials

Research article

The effect of recrystallization annealing on the tungsten surface carbidization in a beam plasma discharge

Mazhyn Skakov[1,3], Victor Baklanov[2], Gainiya Zhanbolatova[1,3,*], Arman Miniyazov[2,4], Igor Sokolov[2,4], Yernat Kozhakhmetov[2], Timur Tulenbergenov[2,4], Nuriya Mukhamedova[2], Olga Bukina[2] and Alexander Gradoboev[5]

[1] National Nuclear Center of the Republic of Kazakhstan, Kurchatov, Kazakhstan
[2] "Institute of Atomic Energy" Branch RSE NNC RK, Kurchatov, Kazakhstan
[3] S. Amanzholov East Kazakhstan University, Ust-Kamenogorsk, Kazakhstan
[4] ShakarimUniversity, Semey, Kazakhstan
[5] National Research Tomsk Polytechnic University, Tomsk, Russia

* **Correspondence:** Email: kaiyrdy@nnc.kz; Tel: +7-707-814-9049.

Abstract: Tungsten was chosen as the plasma facing material (PFM) of the ITER divertor. However, graphite and carbon-graphite materials are used as PFM in some research thermonuclear facilities, including the Kazakhstan materials science tokamak. This circumstance determines the interest in continuing the study of the formation of mixed layers under plasma irradiation. This article is devoted to the study of the effect of preliminary recrystallization annealing on the carbidization of the tungsten surface in a beam-plasma discharge (BPD), which is one of the ways to simulate the peripheral plasma of a tokamak. Experiments on preliminary isochoric and isothermal annealing of tungsten samples were carried out in the mode of direct heating of tungsten samples by an electron beam. The carbidization of tungsten samples after annealing was carried out in a methane atmosphere in the BPD at a temperature of 1000 ℃ for a duration of 3600 s. Optical microscopy (OM) and X-ray diffraction were used to analyze the structure of the tungsten surface. It has been established that differences in the structure arising during recrystallization annealing affect the transfer of carbon atoms in the near-surface area of tungsten and the formation of tungsten carbides (WC or W_2C).

Keywords: recrystallization; tungsten carbide; carbidization; beam-plasma discharge; plasma surface interaction

1. Introduction

The main advantage of choosing tungsten as a plasma-facing material is due to its properties when interacting with plasma, namely, low sputtering ratio and low hydrogen retention. These properties make tungsten a particularly suitable material for the ITER divertor, where the effect of a high particle flux with energies below the sputtering energy of tungsten is expected [1,2]. However, high operating temperatures in the divertor (stationary up to 1200 ℃, and during breakdowns or transients at about 2000 ℃ [3,4]) can significantly change the microstructure of tungsten due to abnormal grain growth and affect the strength of tungsten [5,6]. It should also be noted that the use of an all-tungsten divertor in future fusion reactors will be complicated due to design constraints and high cost [4,7]. Such tokamaks as WEST [8], EAST [9], and JET [10] have already switched to an all-tungsten divertor. Nevertheless, to date, most fusion engineering research reactors use either tungsten coatings deposited on graphite and carbon-graphite materials, or uncoated graphite materials, including the KTM Kazakhstan materials science tokamak [11]. The presence of various materials in the chamber will lead to the formation of mixed W-C layers as a result of tungsten irradiation with eroded carbon atoms, as well as mutual diffusion at high temperatures [12–16].

The research carried out in the works [3–6] shows that during plasma and tungsten surface interaction, an important role is played by the orientation of surface grains, which can cause serious changes in the surface morphology (blistering, bubble formation, radiation damage). Recrystallization annealing is used to improve the mechanical properties and radiation resistance of pure tungsten, which changes the grain size and can modify their crystallographic orientation (texture). This allows for the choice of tungsten for fusion reactors with a suitable preferred orientation to reduce changes in surface morphology during plasma exposure [17–21]. Budayev and co-authors in the work [17] note that the brittle fracture of the recrystallized layer can lead to the formation of submicron size dust particles, which will lead to plasma contamination and its cooling. Changes in the microstructure due to recrystallization annealing should also be expected to affect the formation of mixed W-C layers.

In this regard, the purpose of this research is to study the effect of preliminary recrystallization annealing on the tungsten surface carbidization.

2. Materials and methods

The studies of the effect of preliminary recrystallization annealing on the tungsten surface carbidization were conducted on a plasma-beam installation (PBI). The PBI is a linear simulator with electron-beam plasma generation, which allows combining plasma exposure with electron-beam with a high heat flux, and is also oriented on versatility and the ability for quick changeover to solve various specialized tasks. Depending on the task, it is possible to apply the regime of direct heating of materials by an electron beam and the regime of plasma irradiation in BPD [22–28]. Carbidization of the tungsten surface was also carried out in PBI according to the previously developed method [29–32]. This method makes it possible to study the formation of a mixed W-C layer on the

tungsten surface under conditions of carbon atoms' local transfer along plasma-wetted surfaces due to hydrocarbons.

To study the effect of recrystallization annealing on the formation of a carbidized layer, tungsten of high purity was chosen in the form of a rod ∅10 mm, from which samples were cut in the form of 2.0 ± 0.1 mm thick disks. The prepared samples were subjected to mechanical grinding and polishing to roughness Ra = 0.02 μm from the irradiated side.

The microstructure of the materials was evaluated by optical microscopy (OM). To observe the samples microstructure by the OM method, chemical etching with a mixed solution of hydrofluoric acid and nitric acid in a volume ratio of 1:1 was carried out [33]. Figure 1 shows images of a tungsten sample microstructure in the initial state and after etching. Presented in Figure 1d is an image of the sample surface obtained on a scanning electron microscope, according to which it can be said that tungsten has a fine-grained structure [34].

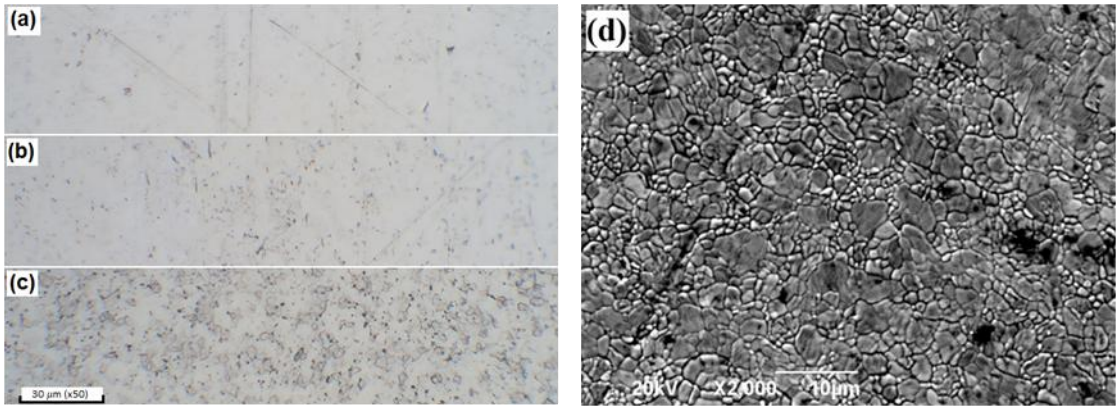

Figure 1. Optical micrographs of a tungsten sample: (a) before etching, (b) after etching for 5 s, (c) after etching for 20 s, (d) SEM image after etching.

For preliminary recrystallization annealing, the mode of direct heating of tungsten samples by an electron beam was used. Isochoric annealing [33] of samples was carried out at three temperatures (1200 ℃, 1300 ℃, 1400 ℃) for 3600 s. Isothermal annealing [33] was also conducted at a temperature of 1400 ℃ with a duration of 1800 s and 3600 s. The choice of these modes is determined by the expected operating conditions in ITER and reference data [35,36].

The pressure in the interaction chamber during annealing was $(1.60 \pm 0.03) \times 10^{-3}$ Pa. After the recrystallization annealing, the Vickers microhardness was measured using a Q60M+ hardness tester (Qness) with an indenter load of 0.2 kgf and a holding time of 10 s. The grain sizes analysis after annealing was carried out using special Axalit software in accordance with ASTM E112-13 [34].

Tungsten surface carbidization after annealing was performed at a temperature of 1000 ℃ with irradiation duration of 3600 s. Two factors were taken into account when selecting the conditions for carbidization experiments. First, in order to reduce the effect of further heat exposure on the microstructure, the temperature of the tungsten surface during carbidization should be lower than the annealing temperature. Second, it was determined in the works [29–32] that the interaction between W and C begins at 1000 ℃ and leads to the formation of tungsten carbides. The pressure of the working gas (CH_4) was $(1.01 \pm 0.04) \times 10^{-1}$ Pa. The ion energy was set by a negative potential on the target node and amounted to 0.5 keV. In this case, the ion current on the target node was 21–23 mA.

Table 1. Sample marking and conditions for conducting experiments on recrystallization annealing and carbidization.

Sample	Recrystallization annealing temperature, °C	Annealing time, s	Surface temperature during carbidization, ℃	Irradiation duration in methane environment, s
DC-1	-	-	1000 ± 10	3600
DC-2	1200 ± 10	3600		
DC-3	1300 ± 10	3600		
DC-4	1400 ± 10	3600		
DC-5	1400 ± 10	1800		

Registration and control of temperature on the front and back sides of the sample's surface was carried out by using pyrometers of the METIS M318 and IMPAC ISR 6 Advanced brands and the VR-5/20 tungsten-rhenium thermocouple, respectively.

The X-ray diffraction patterns of the samples after carbidization for the phase composition determination of the surface were recorded on a diffractometer in Cu-Kα radiation with a PIXcel1D scanning linear detector. The surface phase composition of tungsten samples was identified using the Crystallography Open Database and the PDF-2 ICDD Release 2004 database [37,38]. Diffractometric data cards W_2C No. 03-065-3896, No. 03-065-8829, No. 01-089-2371, WC No. 00-051-0939 as well as card of a metal W No. 00-004-0806 were applied. Quantitative content estimation of phases is determined by the semi-quantitative method of intensity ratio (RIR).

3. Results and discussion

Micrographs presented in Figure 2 shows micrographs were obtained by the OM method of the central region of tungsten samples before and after annealing under different conditions. The microphotographs show the evolution of the tungsten microstructure upon annealing. After reaching the annealing temperature of 1200 ℃, as can be seen from Figure 2b, weakly pronounced low-angle grain boundaries (with the misorientation angle not exceeding 20) and new high-angle grain boundaries (the misorientation angle >20) are observed on the surface, which are characterized by presenting inhomogeneous distribution [39]. Nevertheless, it can be seen that recrystallization nuclei appearance can be noticed mainly along the grain boundaries. According to [40], the size of recrystallized grains is an important characteristic of the annealed material, which can be used to judge the stage of recrystallization: primary, collective, and secondary. The surface microstructure of the DC-3 sample after annealing at 1300 ℃, represented in Figure 2c, corresponds to the grain structure of the primary recrystallization completion stage according to [40]. However, there are recrystallized grains of different sizes, some of them have an approximately equiaxed isometric shape. With an increase in the annealing temperature, microstructures with characteristics of the processes of the collecting and secondary stages of recrystallization are observed (Figure 2d,e). On the surface of the DC-4 and DC-5 samples (Figure 2d,e), which were annealed at a temperature of 1400 ℃, grains of considerable size were found, which was also established by the results of the grain size analysis (see below), and only a small amount of the deformed structure remained. As a result of the rapid migration of high-angle boundaries, recrystallized grains intensively consumed the deformed matrix [39,41].

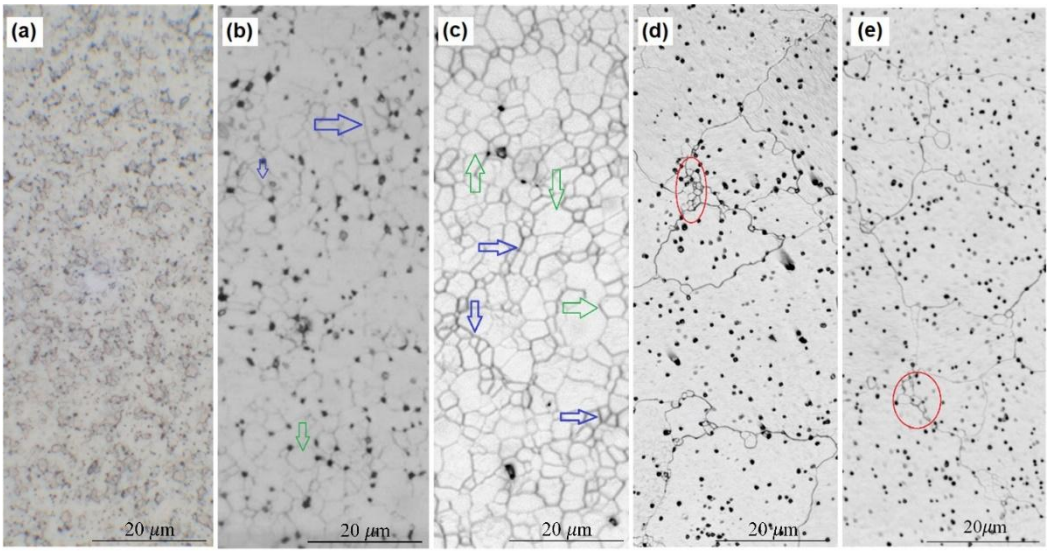

Figure 2. Microstructures of the surface of tungsten samples before and after annealing (central region): a—DC-1, b—DC-2, c—DC-3, d—DC-4, e—DC-5, blue arrows indicate low-angle grain boundaries, green arrows indicate high-angle ones, and red circles indicate areas of the deformed structure.

Edge microstructures of tungsten samples after isochoric annealing are shown in Figure 3. In Figure 3a, obtained from the edge region of DC-4 sample, a migration of high-angle grain boundaries over the entire surface is shown. In the case of the DC-5 sample, which was annealed for 1800 s, high-angle grain boundaries are observed only in the central region of the sample (Figure 2e), while the edge region of the sample retains a fine-grained structure (Figure 3b), which may also indicate different stages of recrystallization.

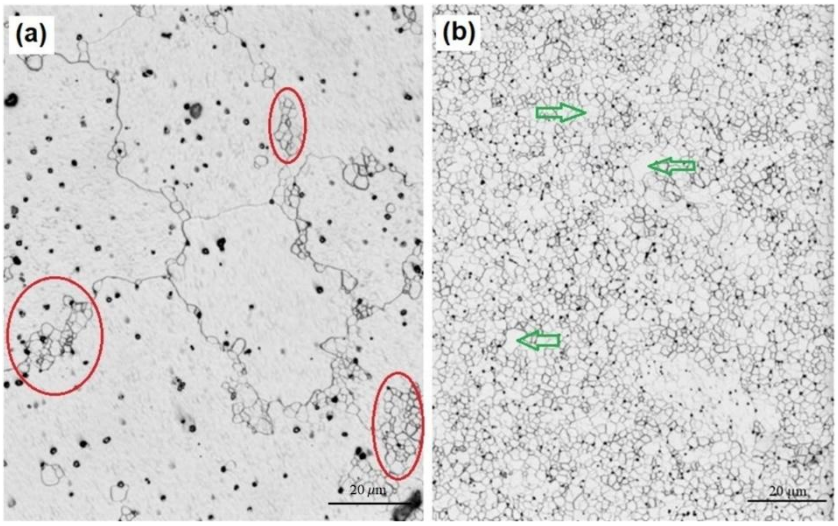

Figure 3. Microstructures of the tungsten samples surface after annealing (edges): a—DC-4, b—DC-5, green arrows indicate high-angle, red circles indicate areas of the deformed structure.

The results of the grain sizes analysis after annealing conducted using the Axalit software, are presented in the form of histograms of the conditional grain sizes distribution in points and their number in Figure 4. According to ASTM E112-13 [34], a smaller value of the grain number corresponds to a larger grain size, and a greater value to a smaller grain size (Table 2).

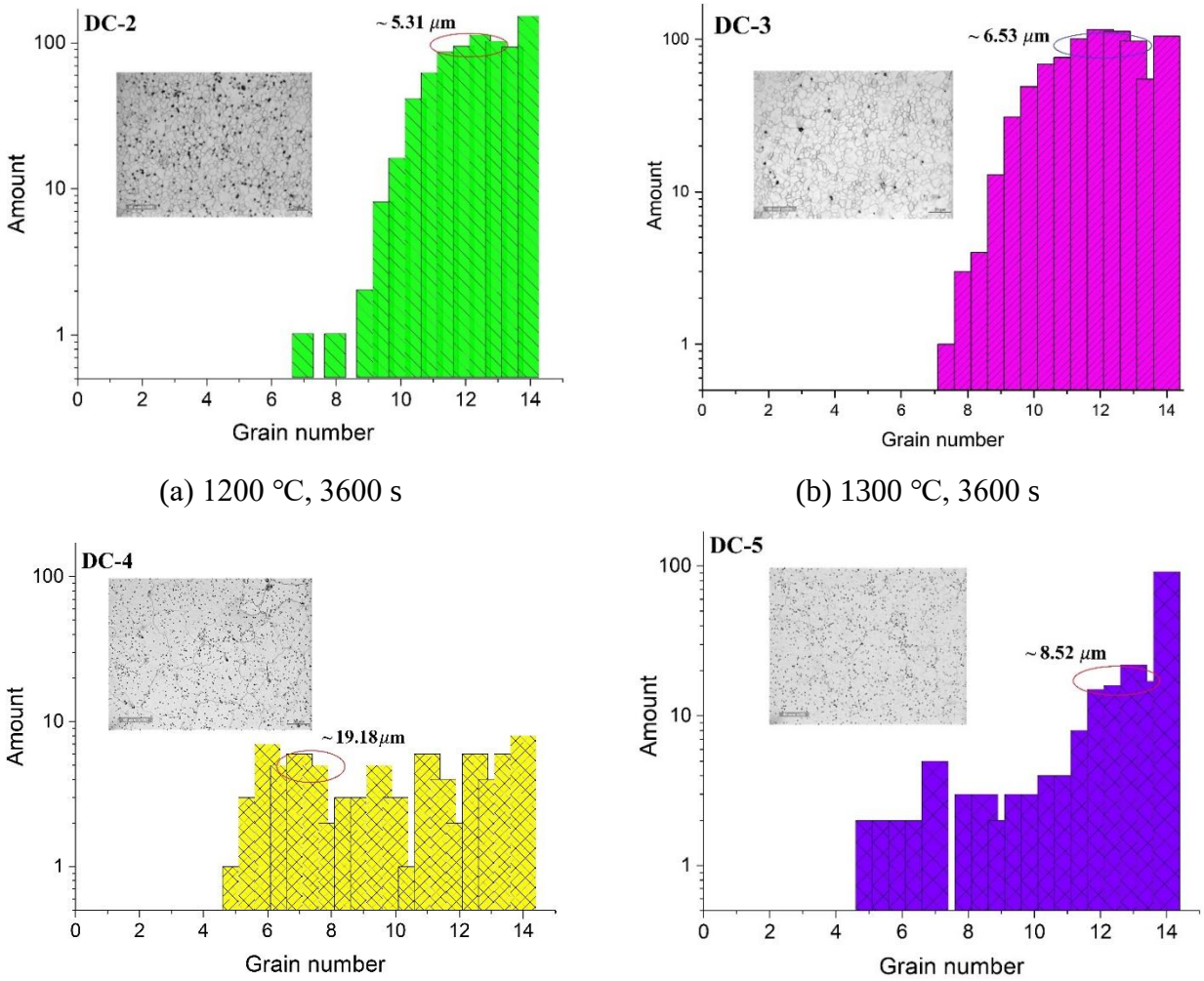

(a) 1200 ℃, 3600 s

(b) 1300 ℃, 3600 s

(c) 1400 ℃, 3600 s

(d) 1400 ℃, 1800 s

Figure 4. Histograms of grain size distribution after annealing.

Table 2. Grain size relationships computed for uniform, randomly oriented, equiaxed grains [34].

Grain size No.	Average diameter
0	359.2
…	…
4.5	75.5
5.0	63.5
5.5	53.4
6.0	44.9
6.5	37.8
7.0	31.8
7.5	26.7
8.0	22.5
8.5	18.9
9.0	15.9
9.5	13.3
10.0	11.2
10.5	9.4
11.0	7.9
11.5	6.7
12.0	5.6
12.5	4.7
13.0	4.0
13.5	3.3
14.0	2.8

As seen in Figure 4, the grain size distribution tends to shift to the left with rise of annealing temperature, which indicates an increase in grain size. The minimum grain size, according to the Axalit software report, after annealing at a temperature of 1200 ℃ comprises 0.29 μm (Figure 4a). The share of these grains is 19.71% of the total number of grains. The proportion of average grain sizes corresponding to 11–13.5 points with an average grain size of ~5.31 μm reaches 63.29%. Primary recrystallization is assumed to happen at this temperature, which is characterized by irregular shape and different grain sizes. The results of the grain sizes analysis confirm that the completion of the stages of primary and the beginning of collective recrystallization occurs with an increase in the annealing temperature to 1300 ℃. Since there is a homogeneous grain growth, as evidenced by the rise in the average grain size to ~6.53 μm, the share of which is equal to 67.02% (Figure 4b). Collective recrystallization is also characterized by the growth of some recrystallized grains by means of neighboring recrystallized grains due to migration of high-angle boundaries [39,40]. A further increase in the annealing temperature to 1400 ℃ results in a uniform increase in the size of recrystallized grains (Figure 4c), which may also indicate collective recrystallization. The proportion of average size grains of ~19.18 μm, corresponding to 8–12.5 points, amounts to 57.5%, while the proportion of large grains was 33.75%. From the histogram in Figure 4d, it can be seen that after annealing for 1800 s, the structure consists of many small grains, the share of

which is 44.02% of the total number of grains, and a small number of very large grains. Such a structure, according to [39,40], resulting from uneven grain growth, is called secondary recrystallization.

Vickers hardness changes during isochoric annealing for 3600 s and isothermal annealing at 1400 ℃ are presented in Figures 5a,b, respectively. As can be seen from Figure 5a, the hardness decreases with the growth of annealing temperature from 486 HV0.2 in the initial state to 389 HV0.2 after annealing at 1400 ℃. Figure 5b shows that the hardness was decreasing with the increase in annealing time. During the annealing process, grain growth occurs due to continuous static recrystallization, which leads to a decrease in hardness according to [42,43].

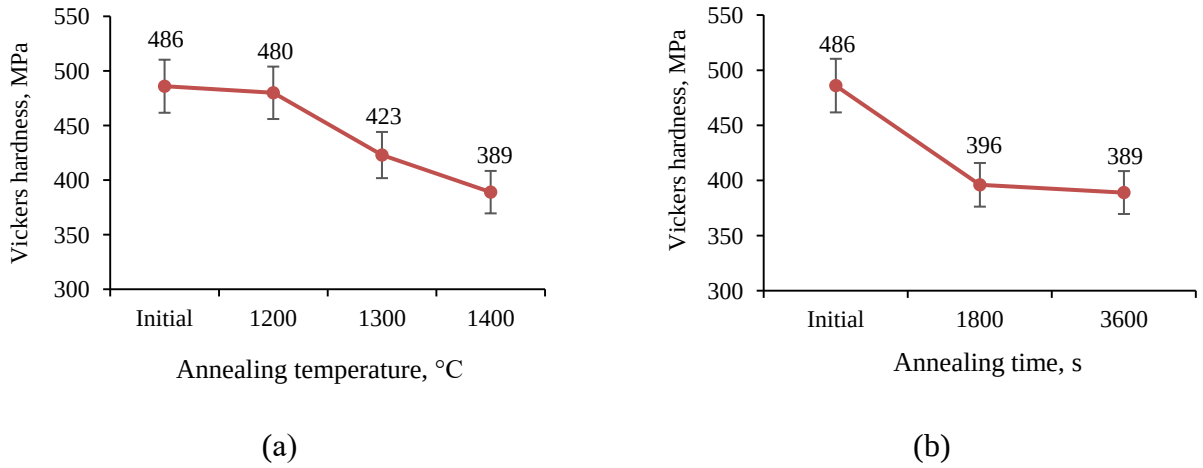

Figure 5. Change in Vickers hardness during isochoric annealing (a) and isothermal annealing (b).

In the process of analyzing the phase composition of the samples surface, when diffractometric data corresponding to the tungsten phase are superimposed on the diffraction pattern of the cards, the experimental peak intensities were noticed to completely coincide with the bar diagram of the used card, despite the complete correspondence of the angular positions. In this regard, to identify the phase composition, diffraction data cards for metallic tungsten No. 00-004-0806, W_2C No. 03-065-3896 and WC No. 00-051-0939 with the most suitable angular positions and having the highest conformity score were applied. The overlay of diffraction patterns before and after the annealing of the tungsten sample is shown in Figure 6.

The state of the crystal structure of tungsten in the initial state is characterized by low intensity and a significant width of the peaks, indicating the distortion of the crystal lattice. Recrystallization annealing leads to an increase in the intensity of the peaks with a shift towards smaller angles and a decrease in their half-width, which points to the formation of a more perfect and homogeneous structure and the decrease in the interplanar spacing [43]. The results of the half-width (FWHM) analysis of the tungsten diffraction line are shown in a diagram in Figure 7.

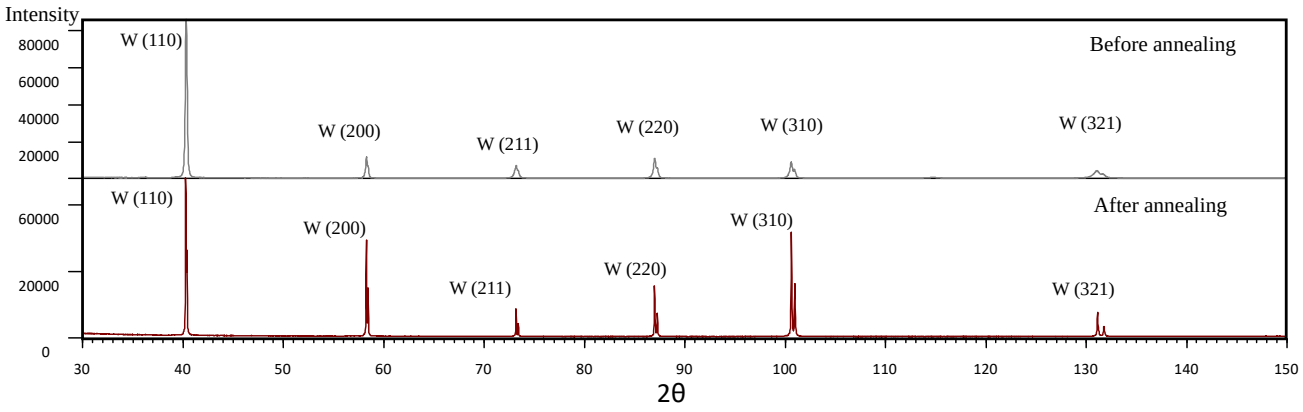

Figure 6. Overlay of X-ray diffraction patterns of a tungsten sample before and after recrystallization annealing.

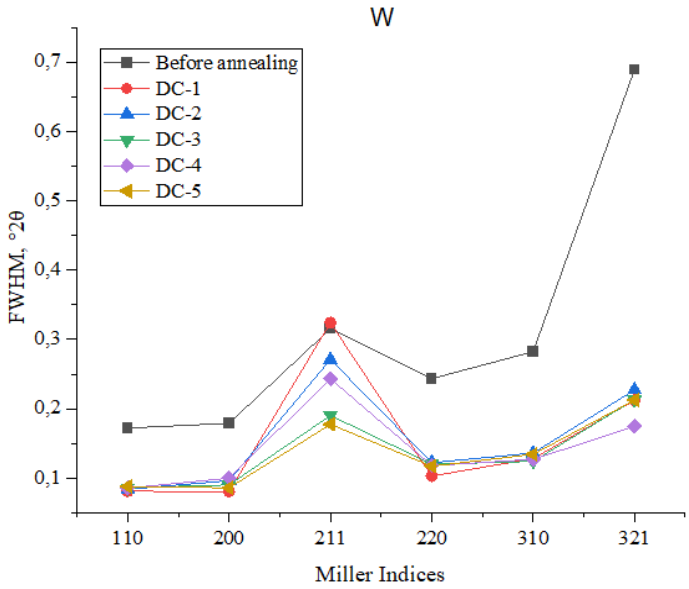

Figure 7. Change of half-width (FWHM) of W lines.

After annealing under different conditions, a noticeable decrease in the half-width of the tungsten diffraction line is observed. However, the half-width of the line corresponding to the tungsten peak with Miller indices (211) after annealing at temperatures of 1200 °C and 1400 °C remains on par with the initial value, which indicates possible microstresses. As the annealing temperature increases, the microstresses disappear and the lowering of half-width takes place.

The overlay of diffraction patterns from the samples after carbidization is presenred in Figure 8. On the obtained diffractograms of the samples, diffraction peaks of WC and W_2C are observed. Taking into account the similarity of the conditions of the diffraction experiment, the visual distinictions in the diffraction patterns indicate differences in the phase composition and structure.

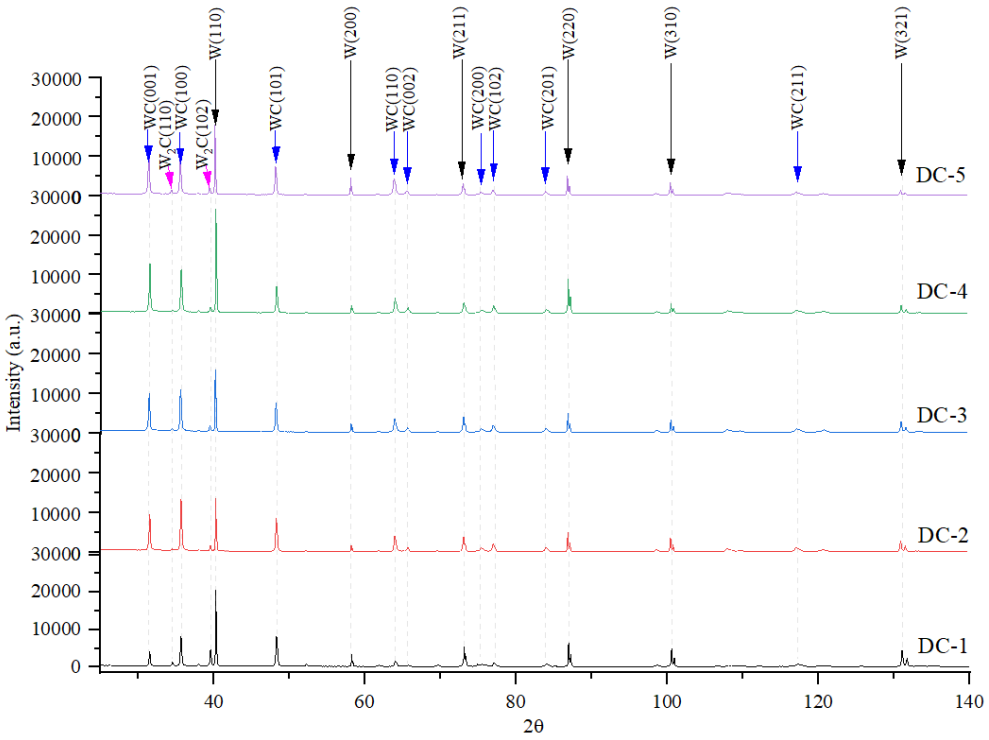

Figure 8. X-ray diffractograms of the samples, Cu ($K_{\alpha 1,2}$) radiation.

In the phase composition of the DC-1 sample, the basis of the phase composition is the crystalline tungsten phase. The second phase in terms of intensity is the WC phase of the hexagonal syngony. The peaks of this phase are characterized by a redistribution of intensities: in accordance with the diffraction data card, the maximum peak of this phase should be dislocated in the region of angles of 35.6°2θ (Miller indices (100)). On the diffraction pattern, the maximum intensity of this phase belongs to the peak at 48.3°2θ (Miller indices (101)). Peaks of low intensity are identified as peaks belonging to the W_2C phase of the hexagonal syngony. In the phase composition of DC-2 sample, the content of the carbide phase and the tungsten phase is almost the same. Peaks of low intensity are also identified as peaks belonging to the W_2C phase of the hexagonal syngony. In the phase composition of DC-3–DC-5 samples, the basis of the phase composition is the phase of crystalline tungsten. The second phase in terms of intensity is the WC phase of the hexagonal syngony. Peaks of low intensity are identified as belonging to the W_2C phase of the hexagonal syngony.

The results of the line widths analysis of tungsten carbides are shown in the form of diagrams in Figure 9. In Figure 9a an increase in the half-width of the WC lines depending on the conditions of preliminary recrystallization annealing is illustrated. The most noticeable broadening of the diffraction lines is noticed for the DC-5 sample annealed at a temperature of 1400 ℃ for 1800 s rather than for the unannealed DC-1 sample. An increase in the half-width of the W_2C lines is also observed depending on the conditions of preliminary recrystallization annealing (Figure 9b). This fact may indicate the distortion of the lattice associated with the processes of structural rearrangement.

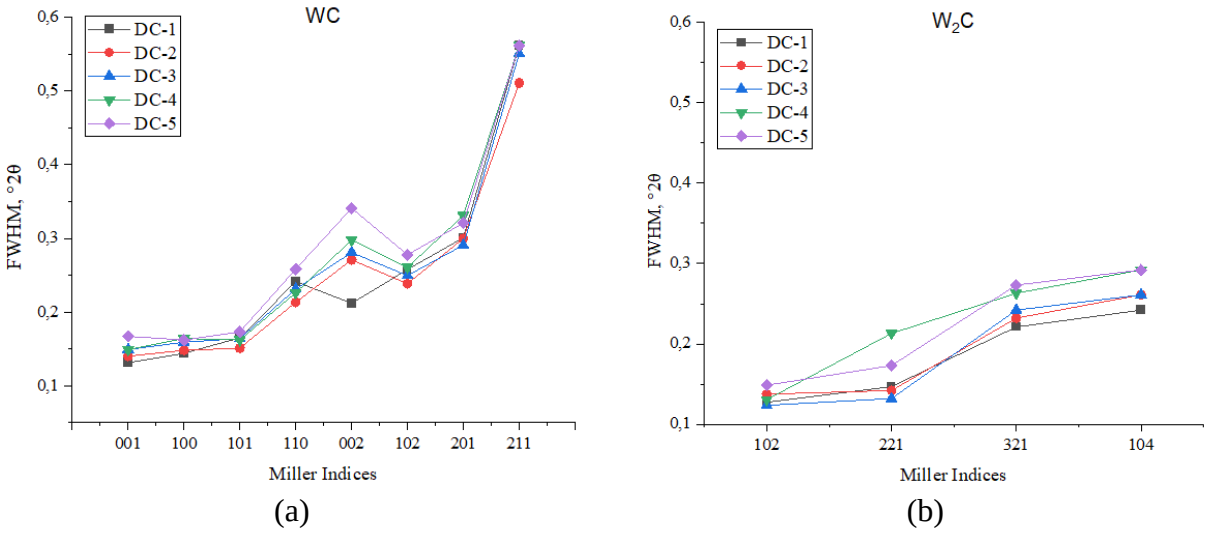

Figure 9. Change of half-width (FWHM) of lines: a—WC, b—W_2C.

The results of the quantitative content assessment are presented in Table 3. Data is given with an accuracy of 0.1% to record the appearance of peaks when the experiment mode is changed.

Table 3. Results of quantitative phase analysis of samples.

Sample	Results of a quantitative assessment of the phases content		
	W (cub.)	WC (hex., P-6m2)	W_2C (hex., P-31m)
DC-1	61.5	22.4	16.1
DC-2	46.1	47.6	6.4
DC-3	54.9	37.4	7.6
DC-4	65.9	29.3	4.8
DC-5	59.6	33.1	7.3

According to the results of X-ray diffraction analysis, it can be found that, under the same conditions of tungsten carbidization, the phase composition of the surface has a noticeable difference. The tungsten phase remains the dominant phase both in the sample irradiated without preliminary recrystallization annealing (DC-1) and in the samples pre-annealed (DC-2–DC-5). However, the samples with preliminary recrystallization annealing show a decrease in the tungsten content, with the exception of the DC-4 sample annealed at a temperature of 1400 °C. All samples present a noticeable increase in the WC phase and a decrease in the W_2C phase relative to the initial tungsten.

4. Conclusions

As part of this research, experiments were conducted to study the effect of recrystallization annealing on the carbidization of the tungsten surface in BPD. The microstructure analysis of the surface of tungsten samples showed that recrystallization nuclei appear mainly along the grain boundaries. With an increase in the annealing temperature to 1400 °C, high-angle grain boundaries

migrate over the entire surface, which indicates normal grain growth and the transition of the whole structure to a recrystallized state. According to the results of the grain sizes analysis after annealing, primary recrystallization is established to take place at a temperature of 1200 ℃, which is characterized by irregular shape and varying sizes of grain. The completion of the stages of primary and the beginning of collective recrystallization is observed with the annealing temperature rise to 1300 ℃. The uniform growth of grains takes place evidenced by an increase in the average grain size to ~6.53 μm, the share of which reaches 67.02%. A further increase in the annealing temperature to 1400 ℃ leads to a homogenous increase in the size of recrystallized grains (Figure 4c), which may also indicate collective recrystallization. However, after being annealed for 1800 s, the structure consists of many small grains, the share of which is 44.02% of the total number of grains, and a small number of very large grains.

According to the results of the Vickers hardness measuring, the decrease in the tungsten surface hardness was established with increasing the annealing temperature from a value of 486 HV0.2 in the initial state to a value of 389 HV0.2 at an annealing temperature of 1400 ℃. The hardness had similar decreasing tendency in relation to the growing annealing time. According to literature data, a drop in hardness is an indicator for the beginning of recrystallization.

The results of the X-ray diffraction phase analysis showed WC and W_2C peaks in the diffraction patterns of samples after carbidization in addition to tungsten peaks. However, after carbidization of the preliminarily annealed samples, a noticeable increase in the content of the WC phase and a decrease in the content of the W_2C phase relative to the initial tungsten can be seen. A comparative analysis of the diffraction line widths of tungsten carbides implied that the most noticeable broadening of the diffraction lines is found in a sample annealed at a temperature of 1400 ℃ for 1800 s, thus indicating a distortion of the lattice related to the processes of structural rearrangement.

It follows that the differences in the structure arising during recrystallization annealing affect the transfer of carbon atoms in the near-surface area of tungsten and the formation of one or another phase of tungsten carbide. However, for a more accurate assessment of the effect of recrystallization annealing of the tungsten sample surface on carbidization, further development of experimental data is necessary.

Use of AI tools declaration

The authors declare they have not used Artificial Intelligence (AI) tools in the creation of this article.

Acknowledgments

This research was conducted within the framework of Program No. BR09158585 “Scientific and technical support of experimental studies at the Kazakhstani Material Testing Tokamak KTM”.

Conflict of interest

The authors declare that they have no known competing financial interests or personal relationships that could have appeared to influence the work reported in this paper.

References

1. Hirai T, Maier H, Rubel M, et al. (2007) R&D on full tungsten divertor and beryllium wall for JET ITER-like wall project. *Fusion Eng Des* 82: 1839–1845. https://doi.org/10.1016/j.fusengdes.2007.02.024
2. Pintsuk G, Hasegawa A (2019) Tungsten as a plasma-facing material, *Reference Module in Materials Science and Materials Engineering*, Elsevier Inc. https://doi.org/10.1016/B978-0-12-803581-8.11696-0
3. Davis JW, Barabash VR, Makhankov A, et al. (1998) Assessment of tungsten for use in the ITER plasma facing components. *J Nucl Mater* 258-263: 308–312. https://doi.org/10.1016/S0022-3115(98)00285-2
4. Castin N, Van den Kerkhof S, Bonny G, et al. (2023) On the microstructure evolution in tungsten ITER monoblocks: A computational study. *Comp Mater Sci* 219: 112001. https://doi.org/10.1016/j.commatsci.2022.112001
5. Xu HY, Zhang YB, Yuan Y, et al. (2013) Observations of orientation dependence of surface morphology in tungsten implanted by low energy and high flux D plasma. *J Nucl Mater* 443: 452–457. https://doi.org/10.1016/j.jnucmat.2013.07.062
6. Jia YZ, Liu W, Xu B, et al. (2016) Mechanism for orientation dependence of blisters on W surface exposed to D plasma at low temperature. *J Nucl Mater* 477: 165–171. https://doi.org/10.1016/j.jnucmat.2016.05.011
7. Wirtz M, Uytdenhouwen I, Barabash V, et al. (2017) Material properties and their influence on the behaviour of tungsten as plasma facing material. *Nucl Fusion* 57: 066018. https://doi.org/10.1088/1741-4326/aa6938
8. Missirlian M, Firdaouss M, Richou M, et al. (2023) Manufacturing, testing and installation of the full tungsten actively cooled ITER-like divertor in the WEST tokamak. *Fusion Eng Des* 193: 113683. https://doi.org/10.1016/j.fusengdes.2023.113683
9. Yu Y, Zhou D, Sakamoto M, et al. (2023) Fuel recycling control in long pulse operation with full tungsten divertors in EAST tokamak. *Nucl Mater Energy* 34: 101333. https://doi.org/10.1016/j.nme.2022.101333
10. Matthews GF, Coad P, Greuner H, et al. (2009) Development of divertor tungsten coatings for the JET ITER-like wall. *J Nucl Mater* 390–391: 934–937. https://doi.org/10.1016/j.jnucmat.2009.01.239
11. Tazhibayeva IL, Azizov EA, Krylov VA, et al. (2017) KTM experimental complex project status. *Fusion Sci Technol* 47: 746–750. https://doi.org/10.13182/FST05-A775
12. Luthin J, Linsmeier C (2000) Carbon films and carbide formation on tungsten. *Surf Sci* 454–456: 78–82. https://doi.org/10.1016/S0039-6028(00)00181-3
13. Samarkhanov K, Batyrbekov E, Khasenov M, et al. (2019) Study of luminescence in noble gases and binary Kr-Xe mixture excited by the products of 6Li(N, α)T nuclear reaction. *Eurasian Chem-Technol* 21: 115–123. https://doi.org/10.18321/ectj821
14. Linsmeier Ch, Luthin J, Klages KU, et al. (2004) Formation and erosion of carbon-containing mixed materials on metals. *Phys Scripta* T111: 86–91. https://doi.org/10.1238/Physica.Topical.111a00086

15. Linsmeier Ch, Reinelt M, Schmid K (2011) Surface chemistry of first wall materials—From fundamental data to modeling. *J Nucl Mater* 415: S212–S218. https://doi.org/10.1016/j.jnucmat.2010.08.056
16. Ponkratov YU, Nikitenkov N, Tazhibayeva I, et al. (2019) Methodology of the experiments to study lithium cps interaction with deuterium under conditions of reactor irradiation. *Eurasian Chem-Technol* 21: 107–113. https://doi.org/10.18321/ectj820
17. Budaev VP, Martynenko YV, Karpov AV, et al. (2015) Tungsten recrystallization and cracking under ITER-relevant heat loads. *J Nucl Mater* 463: 237–240. https://doi.org/10.1016/j.jnucmat.2014.11.129
18. Parish CM, Hijazi H, Meyer HM, et al. (2014) Effect of tungsten crystallographic orientation on He-ion-induced surface morphology changes. *Acta Mater* 62: 173–181. https://doi.org/10.1016/j.actamat.2013.09.045
19. Alfonso A, Jensen DJ, Luo GN, et al. (2014) Recrystallization kinetics of warm-rolled tungsten in the temperature range 1150–1350 ℃. *J Nucl Mater* 455: 591–594. https://doi.org/10.1016/j.jnucmat.2014.08.037
20. Rieth M, Hoffmann A (2010) Influence of microstructure and notch fabrication on impact bending properties of tungsten materials. *Int J Refract Met Hard Mater* 28: 679–686. https://doi.org/10.1016/j.ijrmhm.2010.04.010
21. Mathaudhu SN, de Rosset A J, Hartwig KT, et al. (2009) Microstructures and recrystallization behavior of severely hot-deformed tungsten. *Mater Sci Eng A* 503: 28–31. https://doi.org/10.1016/j.msea.2008.03.051
22. Kolodeshnikov AA, Zuev VA, Ganovichev DA, et al. (2016) Imitation stand with a plasma-beam installation. Republic of Kazakhstan Patent No. 2016/0108.2 (in Russian).
23. Tulubayev Y, Ponkratov Y, Gordienko Y, et al. (2023) Development of a methodology for conducting experiments with a sample of lithium capillary-porous structure at a plasma-beam installation. *Mater Today Proc* 81: 1209–1215. https://doi.org/10.1016/j.matpr.2023.03.176
24. Skakov M, Miniyazov A, Batyrbekov E, et al. (2022) Influence of the carbidized tungsten surface on the processes of interaction with helium plasma. *Materials* 15: 7821. https://doi.org/10.3390/ma15217821
25. Sokolov IA, Skakov MK, Miniyazov AZ, et al. (2021) Interaction of plasma with beryllium. *J Phys-Conf Ser* 2064: 012070. https://doi.org/10.1088/1742-6596/2064/1/012070
26. Skakov M, Batyrbekov E, Sokolov I, et al. (2022) Influence of hydrogen plasma on the surface structure of beryllium. *Materials* 15: 6340. https://doi.org/10.3390/ma15186340
27. Kozhakhmetov Ye, Skakov M, Wieleba W, et al. (2020) Evolution of intermetallic compounds in Ti–Al–Nb system by the action of mechanoactivation and spark plasma sintering. *AIMS Mater Sci* 7: 182–191. https://doi.org/10.3934/matersci.2020.2.182
28. Mukhamedova N, Kozhakhmetov Y, Skakov M, et al. (2022) Microstructural stability of a two-phase (O + B2) alloy of the Ti–25Al–25Nb system (at.%) during thermal cycling in a hydrogen atmosphere. *AIMS Mater Sci* 9: 270–282. https://doi.org/10.3934/matersci.2022016
29. Zhanbolatova GK, Baklanov VV, Tulenbergenov TR, et al. (2020) Carbidization of the tungsten surface in a beam-plasma discharge. *NNC RK Bulletin* 4: 77–81 (in Russian).
30. Baklanov V, Zhanbolatova G, Skakov M, et al. (2022) Study of the temperature dependence of a carbidized layer formation on the tungsten surface under plasma irradiation. *Mater Res Express* 9: 016403. https://doi.org/10.1088/2053-1591/ac4626

31. Zhanbolatova GK, Baklanov VV, Skakov MK, et al. (2021) Influence of temperature on tungsten carbide formation in a beam plasma discharge. *J Phys-Conf Ser* 2064: 012055. https://doi.org/10.1088/1742-6596/2064/1/012055
32. Miniyazov AZ, Skakov MK, Tulenbergenov TR, et al. (2021) Investigation of tungsten surface carbidization under plasma irradiation. *J Phys-Conf Ser* 2064: 012053. https://doi.org/10.1088/1742-6596/2064/1/012053
33. Kolenko YA (1994) *Technology of Laboratory Experiment: Handbook*, Polytechnic, 751 (in Russian).
34. ASTM International (2021) Standard test methods for determining average grain size. ASTM E112-13.
35. Bochvar AA (1940) *Fundamentals of Heat Treatment of Alloys*, Metallurgical Publishing House, NKCM Soviet Union, National. Science and technology. Understanding History: Biography Black and Nonferrous Metallurgy, 299 (in Russian). Available from: http://www.e-heritage.ru/Catalog/ShowPub/5078.
36. Aleksandrov VM (2015) *Material Science and Technology of Structural Materials. Part 1: Materials Science*. Arkhangelsk: Northern (Arctic) Federal University, 327 (in Russian). Available from: https://www.studmed.ru/aleksandrov-v-m-materialovedenie-i-tehnologiya-konstrukcionnyh-materialov-uchebnoe-posobie-chast-1-materialovedenie-standart-tretego-pokoleniya_4f2b3ab2370.html.
37. Gražulis S, Chateigner D, Downs RT, et al. (2009) Crystallography Open Database—an open-access collection of crystal structures. *J Appl Cryst* 42: 726–729. https://doi.org/10.1107/S0021889809016690
38. Bukina OS, Kukushkin IM (2019) Identification of changes in the structure and phase composition of the surface layer of tungsten, which occurred as a result of exposure to methane plasma. *NNC RK Bulletin* 3: 46–53 (in Russian).
39. Perevezentsov VN, Shcherban MY (2000) *Recrystallization of Metals and Alloys*, Nizhny Novgorod: Publishing House of the UNN. N.I. Lobachevsky, 62 (in Russian).
40. Gorelik SS, Dobatkin SV, Kaputkina LM (2005) *Recrystallization of Metals and Alloys*, Moscow: MISIS, 432 (in Russian).
41. Zhang ZX, Chen DS, Han WT, et al. (2015) Irradiation hardening in pure tungsten before and after recrystallization. *Fusion Eng Des* 98: 2103–2107. https://doi.org/10.1016/j.fusengdes.2015.06.192
42. Wang K, Sun H, Zan X, et al. (2020) Evolution of microstructure and texture of moderately warm-rolled pure tungsten during annealing at 1300 ℃. *J Nucl Mater* 540: 152412. https://doi.org/10.1016/j.jnucmat.2020.152412
43. Xue K, Guo Y, Zhou Y, et al. (2021) Thermal stability of the HPT-processed tungsten at 1250–1350 ℃. *Int J Refract Met H* 94: 105377. https://doi.org/10.1016/j.ijrmhm.2020.105377

AIMS Press